Modeling of Solidification Process and Investigation of Heat Transfer Mechanisms in Micron-Sized Spherical Cu Particles

PENGYU LI, SIFAN TANG, YIXIN YUE, MAN YAO, XUDONG WANG, and WEI DONG

Pulsated Orifice Ejection Method (POEM) is a typical containerless heat transfer and solidification process for preparing micron-sized spherical particles. The heat transfer mechanisms dominated by convection and radiation are crucial for the preparation process, solidification process, and microstructure control. In this paper, a numerical calculation model for particle heat transfer and solidification in a three-dimensional spherical coordinate system was established to investigate the heat transfer and solidification characteristics of micron-sized metal particles prepared by the POEM. The temperature distribution, variation, and solidification process of the particles during the preparation process were calculated and analyzed, and the relationship between grain size and cooling rate for particles with different diameters was discussed. In addition, the influence and contribution of convection and radiation on the surface heat flux density of the particles were simulated and analyzed. This research provides references for optimizing the preparation process and solidification microstructure of micron-sized spherical particles using the POEM.

I. INTRODUCTION

MICRON-SIZED spherical particles, with sizes ranging from 1 to 1000 μm, are widely used in additive manufacturing,[1,2] electronic packaging,[3] biomedical applications,[4] and other fields. The current methods for particle preparation include Gas Atomization (GA)[5–10] based on droplet spray solidification, Uniform Droplet Spray (UDS),[11–13] and Pulsated Orifice Ejection Method (POEM).[14–17] Achieving narrow particle size distribution, high surface roundness, and uniform microstructure of metal spherical particles is a current research focus and challenge. The solidification time of micron-sized spherical particles is extremely short, and the cooling rate can exceed 10^3 K/s. The solidification process is highly sensitive to thermal shocks. The heat transfer conditions during droplet superheating, nucleation, and solidification significantly affect the advancement of the liquid–solid interface and the resulting microstructure. Given the difficulty of directly monitoring the particle preparation process, modeling and numerical calculations have become important approaches for studying particle heat transfer and solidification behavior.

Song et al.[18] established a numerical heat transfer model for preparing Fe–6.5 pctSi metal particles using atomization method based on the Newtonian heat transfer formula and non-uniform nucleation theory. They studied the temperature variation of the droplets and the solidification characteristics, revealing the relationship between cooling rate and secondary dendrite arm spacing. Yodoshi[19] developed a particle heat transfer model based on Newton's cooling law and calculated the critical cooling rate for the formation of a completely amorphous phase in $Fe_{76}Si_9B_{10}P_5$ alloy micro-particles. Gianoglio et al.[20] used gas atomization to prepare Al–4.5 pct Cu alloy particles and examined the relationship between interdendritic spacing, cooling rate, and particle size using the established numerical heat transfer model. Wang et al.[21] combined Newton's heat transfer formula with the classical heat conduction equation to simulate the free-falling of droplets in a

PENGYU LI and XUDONG WANG are with the School of Materials Science and Engineering, Dalian University of Technology, Dalian 116024, P.R. China and also with the Key Laboratory of Solidification Control and Digital Preparation Technology (Liaoning Province), Dalian University of Technology, Dalian 116024, P.R. China. Contact e-mail: hler@dlut.edu.cn SIFAN TANG, YIXIN YUE, MAN YAO, and WEI DONG are with the School of Materials Science and Engineering, Dalian University of Technology. Contact e-mail: w-dong@dlut.edu.cn

droplet tube, revealing the connection between the thermal properties of metal and gas and the heat transfer process.

The aforementioned studies typically assume that the droplet temperature is uniform, neglecting the non-uniform distribution of temperature and temperature gradients during particle cooling.[22–24] However, experimental data indicate that significant differences exist in the radial solidification microstructure of spherical particles, particularly in cases where the metal has poor thermal conductivity or the cooling rate is low. These research findings deviate from the actual heat transfer and solidification processes of the particles.

In this study, focusing on the heat transfer and solidification characteristics of micron-sized spherical particles prepared by the POEM, a numerical calculation model describing the heat transfer and solidification processes of copper particles in a three-dimensional spherical coordinate system was established. The temperature variation and heat transfer-solidification characteristics during the particle cooling process were accurately computed. Moreover, a comprehensive examination of the relationship between grain size and cooling rate was performed, and the dominant mechanisms affecting particle heat transfer were identified. The findings of this research offer valuable insights for comprehending and effectively controlling the preparation process of micron-sized spherical particles using the POEM.

II. PRINCIPLE AND EXPERIMENTAL RESULTS OF POEM

POEM is a technique used for the on-demand ejection of micron-sized spherical metal particles. The resulting particles have characteristics such as uniform particle size, high surface roundness, and consistent thermal history. The pulsed orifice ejection equipment consists of six main components: a vacuum system, temperature control, differential pressure control, piezoelectric ceramic driving system, particle ejection system, and collection system, as shown in Figure 1. The vacuum system evacuates the air from the chamber, maintaining a low oxygen environment for the experiment. The temperature control system is used to control the heating temperature and holding time of the metal, ensuring the stability of the metal melt temperature. The differential pressure control system controls the differential pressure inside and outside the crucible to ensure the stability and consistency of droplet formation. The piezoelectric ceramic driving system converts electrical signals into mechanical vibration signals, driving the displacement of the transmission rod. The particle ejection system consists of the transmission rod and micro-orifices. The reciprocating motion of the transmission rod causes fluctuations on the surface of the metal melt, forming micro-droplets. The preparation frequency can reach up to 1000 Hz, and the micro-orifices are used to control the size and quantity of the droplets. Finally, the collection system consists of a cooling chamber and a particle collector, which serves to cool the droplets and collect the microspheres.
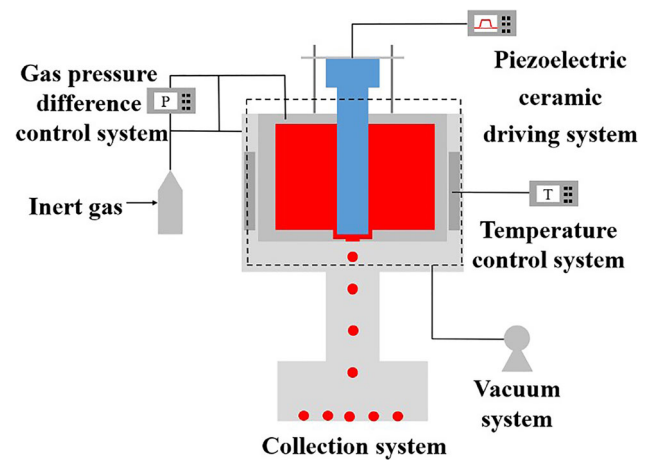

Fig. 1—Schematic diagram of the preparation device by POEM.

The collected particles are placed under an optical microscope, and the morphology of the particles is observed by illuminated from the bottom. Meanwhile, image analysis software Winroof is used to measure the particle diameter and standard deviation, as shown in Figure 2. The standard deviations for particles with diameters of 150, 200, 300, and 400 μm are 8.28, 2.02, 4.31, and 3.22 μm, respectively. It can be observed that the particles prepared by the POEM have the advantages of high sphericity and uniform particle size. The following sections will focus on modeling, calculating, and analyzing the heat transfer and solidification behavior of spherical particles with different diameters.

III. MATHEMATICAL MODEL

A. Simplifications and Assumptions

During the preparation of micron-sized spherical particles using the POEM, the molten metal is subjected to forced disturbance due to the combined effect of the pressure difference inside and outside the crucible and the transmission rod. When the energy of the disturbance exceeds the additional stress caused by surface tension at the liquid surface of the micro-orifice, certain amount of the metal melt is ejected from the micro-orifice. The separated metal liquid, under the influence of vibration and surface tension, forms spherical micro-droplets. These droplets then undergo cooling and solidification under the protection of an inert gas, resulting in the formation of spherical particles. In order to study the heat transfer and solidification characteristics during the particle formation process, appropriate simplifications and assumptions are made in the model.

(1) The particles are considered as complete spheres, neglecting any contraction or deformation during the solidification process.
(2) The particles are assumed to be in a nearly gravity-free state during their descent, disregarding the gas drag force acting on the particles.

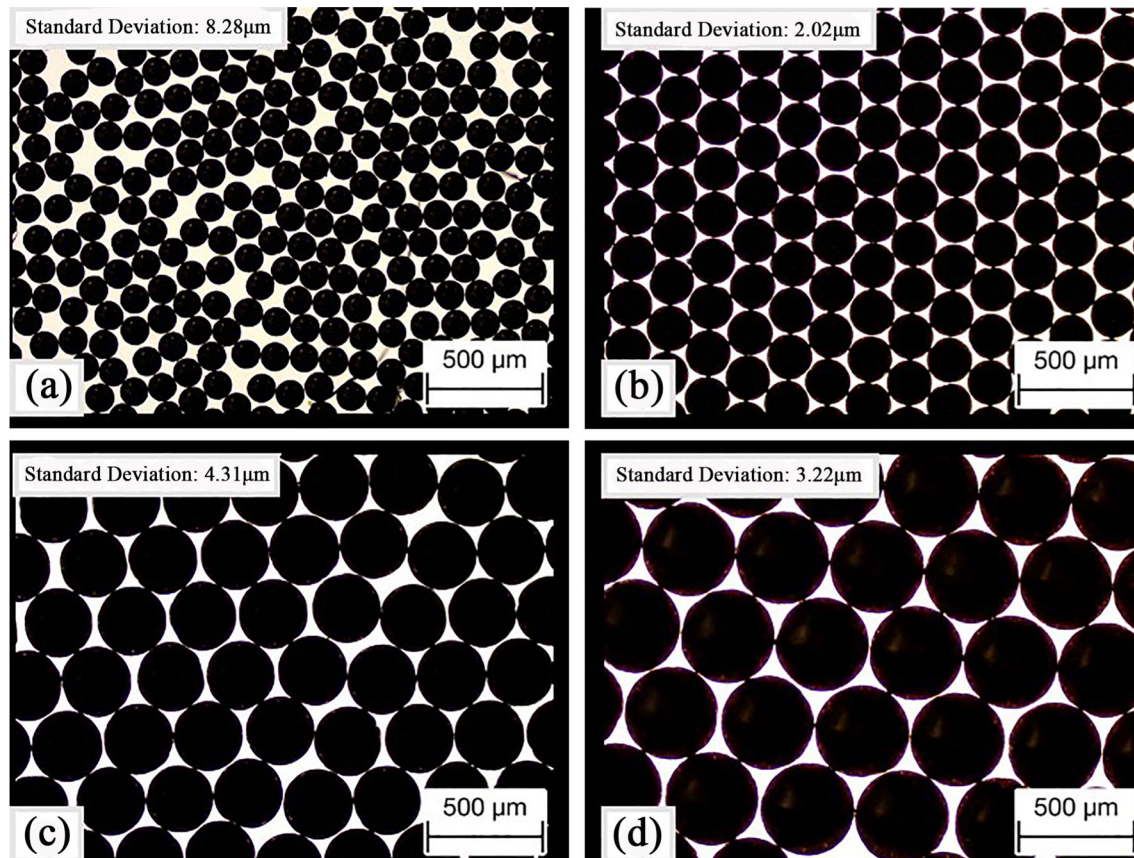Fig. 2—Copper particles with different diameters and their standard deviation: (*a*) 150 *μ*m; (*b*) 200 *μ*m; (*c*) 300 *μ*m; (*d*) 400 *μ*m.

(3) The influence of convective heat transfer within the molten metal is neglected, considering only conductive heat transfer.

(4) The heat transfer conditions on the surface of the particles are assumed to be uniform.

(5) The temperature of the inner wall of the cooling chamber is assumed to be constant and equal to the temperature of the cooling water.

(6) The material properties such as density, specific heat, and thermal conductivity of the metal are considered to vary with temperature.

Table I provides a list of nomenclature, parameters, and their respective units for each variable in this study.

B. Numerical Heat Transfer-Solidification Model

1. Droplet velocity

During the droplet falling process, it undergoes uniformly accelerated linear motion under the influence of gravity. Its motion behavior can be described by the following dynamic equation.

$$v_t = v_0 + g t_t \qquad [1]$$

$$t_t = \left(\sqrt{v_0^2 + 2 g h_t} - v_0 \right) \Big/ g, \qquad [2]$$

where g is the acceleration due to gravity, with a value of 9.81.

2. Heat transfer model for droplets

During the falling process of the droplet inside the cooling chamber, it does not come into contact with the container or the mold, making it a typical unconstrained and non-contact special solidification process. During this process, convection and radiation heat transfer occur between the droplet, cooling gas, and the inner wall of the chamber. Previous studies on powder preparation using atomization methods assumed a uniform temperature distribution inside the droplet without temperature gradients. However, temperature gradients are the dominant factors affecting dendritic growth and solidification microstructure. As the droplet size increases, significant differences in solidification microstructure occur radially, rendering the previous

Table I. All Terms in the Paper

Nomenclature	Parameters (Unit)
v	velocity (m/s)
g	gravitational acceleration (m/s)
t	time (s)
h	height (m)
c_p	specific heat capacity [J/(kg °C)]
T	temperature (°C)
Q	internal heat source (J)
L	latent heat of solidification (kJ/kg)
q	heat flow (W/m²)
h	convective heat transfer coefficient [W/(m² °C)]
d	cooling equivalent length (m)
k	thermal conductivity [W/(m °C)]
Δr	radial space step (μm)
$\Delta \theta$	zenith angle direction space step (rad)
$\Delta \varphi$	azimuth direction space step (rad)
$\Delta \tau$	time step (s)
$dT \cdot dt^{-1}$	cooling rate (°C/s)
D	particle diameter (μm)
λ^2	secondary dendrite arm spacing (μm)
ρ	density (kg/m³)
λ	thermal conductivity of metal [W/(m °C)]
μ	viscosity (N s/m²)
β	material constants
ε	emissivity
σ	Stefan–Boltzmann constant [W/(m² °C⁴)]
α	thermal diffusivity (m² s)
L(Subscript)	liquid
S(Subscript)	solid
conv(Subscript)	convection
rad(Subscript)	radiation
g(Subscript)	gas
m(Subscript)	metal particle
i(Subscript)	unit number
j(Subscript)	unit number
k(Subscript)	unit number
w(Subscript)	wall
p(Superscript)	last moment
p + 1(Superscript)	next moment
*(Superscript)	consider latent heat release

model inapplicable. It is necessary to establish a transient numerical model for heat transfer and solidification processes of the droplets, in order to reveal the heat transfer characteristics and patterns during particle solidification and provide support for understanding and controlling the solidification microstructure of the particles.

In a three-dimensional spherical coordinate system, the center of the droplet is placed at the origin of the coordinate system. The grid is divided into r, θ, and φ directions, where r, θ, φ are the radial distance, the zenith angle, and the azimuth angle. Their respective ranges are $r \in [0, +\infty)$, $\theta \in [0, \pi]$, and $\varphi \in [0, 2\pi]$. The

droplet is divided into different volume elements, as shown in Figure 3. The internal volume elements of the microdroplet are represented by ABCD-A′B′C′D′.

The heat transfer governing equation can be described as follows:

$$\frac{\partial}{\partial t}(\rho c_p T) = \frac{1}{r^2}\frac{\partial}{\partial r}\left(\lambda r^2 \frac{\partial T}{\partial r}\right) + \frac{1}{r^2 \sin^2 \theta}\frac{\partial}{\partial \varphi}\left(\lambda \frac{\partial T}{\partial \varphi}\right) + \frac{1}{r^2 \sin \theta}\frac{\partial}{\partial \theta}\left(\lambda \sin \theta \frac{\partial T}{\partial \theta}\right) + Q. \quad [3]$$

3. Treatment of latent heat of solidification

In this paper, the calculated material is pure metal. Therefore, the temperature recovery method is used to handle the release of crystallization latent heat. Assuming that the latent heat is released linearly, when $T^p \geq T_L$ and $T^{p+1} \geq T_S - L/C_p$, the temperature of the pure metal at the next moment during the solidification process can be described as follows:

$$\left(T^{p+1}\right)^* = \frac{T_L \cdot L + T^{p+1} \cdot c_p \cdot (T_L - T_S)}{L + c_p \cdot (T_L - T_S)}. \quad [4]$$

In the case of pure metal, the solidus temperature and liquidus temperature are the same, so the compensatory temperature change is expressed as the difference between the liquidus temperature and the uncompensated temperature at the current moment.

C. Initial and boundary conditions

For the initial conditions in the calculations, the temperature of the metal melt in the crucible is maintained at $T_0 = T_m + 20$ °C. The temperature of the inert gas in the cooling chamber is the same as the temperature of the chamber walls, which is $T_g = T_w = 20$ °C. The initial velocity of the droplet when it is ejected from the orifice is $v_0 = 2$ m/s.

During the droplet cooling process, there is no contact with the container or mold, and evaporation is not considered. The droplet's surface is subject to convective and radiative heat transfer mechanisms, as shown in Eq. [5]. The heat transferred from the droplet's surface to the inert gas follows Newton's cooling law, as described in Eq. [6]. The heat transferred from the droplet's hot surface to the chamber wall due to radiative effects can be considered using Eq. [7].

$$q_{total} = q_{rad} + q_{conv} \quad [5]$$

$$q_{conv} = -h(T - T_g) \quad [6]$$

$$q_{rad} = \varepsilon \sigma (T^4 - T_w^4), \quad [7]$$

where ε is the emissivity or radiative property of the droplet, and in this study, it is assumed to be 0.8, σ is the Stefan–Boltzmann constant, with a numerical value of 5.67×10^{-8}.
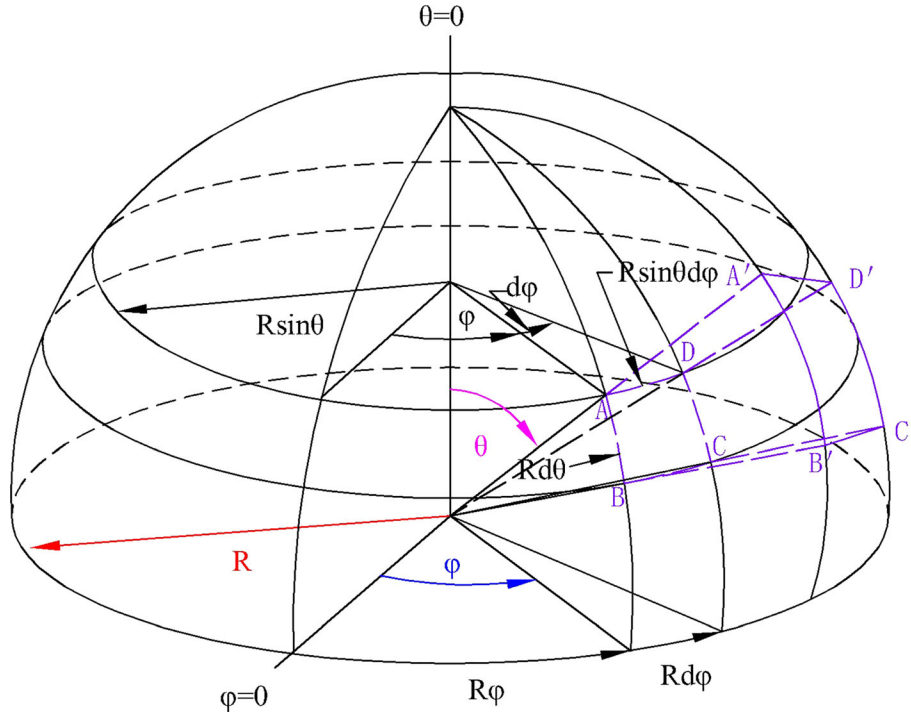
Fig. 3—Schematic diagram of subdivision unit body in spherical coordinate system.

It is assumed that the heat transfer conditions for a falling droplet in a quiescent gas are the same as those for a stationary droplet in a forced convection environment. The heat transfer coefficient h can be determined using the Ranz–Marshall equation, an empirical relationship that is effective for calculating single spherical droplets moving in a uniformly accelerated linear motion in the cooling chamber when Re ≤ 1000.[23,25]

$$h = \frac{k_g}{d}\left(2.0 + 0.6\sqrt{\mathrm{Re}}\sqrt[3]{\mathrm{Pr}}\right) \qquad [8]$$

$$\mathrm{Re} = \rho_g d v_m / \mu_g \qquad [9]$$

$$\mathrm{Pr} = c_{pg}\mu_g / k_g, \qquad [10]$$

where Re is the Reynolds number and Pr is the Prandtl number.

D. Equation Discretization and Stability Conditions

When dealing with physical problems described by partial differential equations with complex initial and boundary conditions, obtaining analytical solutions can be difficult. Therefore, in this work, a finite difference method with an explicit scheme is used to discretize the heat transfer control equation. The particle is divided into grids in the radial, zenith angle, and azimuthal directions. Forward differencing is used for the time derivative, while central differencing is used for the spatial derivatives. This leads to the discretization equation for the internal cells (Eq. [11]) and the boundary cells (Eq. [12]).

$$
\begin{aligned}
T_{i,j,k}^{p+1} =& \frac{\alpha\left(r_{i,j,k}+\Delta r/2\right)^2 \Delta\tau}{\left(r_{i,j,k}\cdot\Delta r\right)^2}T_{i+1,j,k}^p + \frac{\alpha\left(r_{i,j,k}-\Delta r/2\right)^2 \Delta\tau}{\left(r_{i,j,k}\cdot\Delta r\right)^2} \\
& T_{i-1,j,k}^p + \frac{\alpha\sin\left(\theta_{i,j,k}+\Delta\theta/2\right)\cdot\Delta\tau}{\sin\theta_{i,j,k}\left(r_{i,j,k}\Delta\theta\right)^2}T_{i,j+1,k}^p + \frac{\alpha\sin\left(\theta_{i,j,k}-\Delta\theta/2\right)\Delta\tau}{\sin\theta_{i,j,k}\left(r_{i,j,k}\Delta\theta\right)^2}T_{i,j-1,k}^p \\
& + \frac{\alpha\Delta\tau}{\left(r_{i,j,k}\cdot\sin\theta_{i,j,k}\cdot\Delta\varphi\right)^2}\left(T_{i,j,k+1}^p + T_{i,j,k-1}^p\right) \\
& + \left(1 - \frac{\alpha\Delta\tau}{\left(r_{i,j,k}\cdot\Delta r\right)^2}\left(\left(r_{i,j,k}+\Delta r/2\right)^2 + \left(r_{i,j,k}-\Delta r/2\right)^2\right) - \frac{\alpha\cdot\Delta\tau}{\sin\theta_{i,j,k}\left(r_{i,j,k}\Delta\theta\right)^2}\right. \\
& \left(\sin\left(\theta_{i,j,k}+\Delta\theta/2\right) + \sin\left(\theta_{i,j,k}-\Delta\theta/2\right)\right) - \left. \frac{2\alpha\Delta\tau}{\left(r_{i,j,k}\cdot\sin\theta_{i,j,k}\cdot\Delta\varphi\right)^2}\right) T_{i,j,k}^p
\end{aligned}
$$

[11]

$$
\begin{aligned}
T_{i,j,k}^{p+1} =& \frac{q}{\rho c_p}\cdot\frac{\left(r_{i,j,k}+\Delta r/2\right)^2\cdot\Delta\tau}{r_{i,j,k}^2\cdot\Delta r} + \frac{\alpha\left(r_{i,j,k}-\Delta r/2\right)^2\Delta\tau}{\left(r_{i,j,k}\cdot\Delta r\right)^2}T_{i-1,j,k}^p \\
& + \frac{\alpha\cdot\sin\left(\theta_{i,j,k}+\Delta\theta/2\right)\Delta\tau}{\sin\theta_{i,j,k}\left(r_{i,j,k}\Delta\theta\right)^2}T_{i,j+1,k}^p + \frac{\alpha\cdot\sin\left(\theta_{i,j,k}-\Delta\theta/2\right)\Delta\tau}{\sin\theta_{i,j,k}\left(r_{i,j,k}\Delta\theta\right)^2}T_{i,j-1,k}^p \\
& + \frac{\alpha\Delta\tau}{\left(r_{i,j,k}\cdot\sin\theta_{i,j,k}\cdot\Delta\varphi\right)^2}\left(T_{i,j,k+1}^p + T_{i,j,k-1}^p\right) + \left(1 - \frac{\alpha\left(r_{i,j,k}-\Delta r/2\right)^2\Delta\tau}{\left(r_{i,j,k}\cdot\Delta r\right)^2}\right. \\
& - \frac{\alpha\cdot\Delta\tau}{\sin\theta_{i,j,k}\left(r_{i,j,k}\Delta\theta\right)^2}\left(\sin\left(\theta_{i,j,k}+\Delta\theta/2\right) + \sin\left(\theta_{i,j,k}-\Delta\theta/2\right)\right) \\
& \left. - \frac{2\alpha\Delta\tau}{\left(r_{i,j,k}\cdot\sin\theta_{i,j,k}\cdot\Delta\varphi\right)^2}\right)T_{i,j,k}^p
\end{aligned}
$$

[12]

Table II. Physical Parameters of TU2 Oxygen-Free Copper

Parameter (Unit)	Value
Thermal Conductivity [W/(m °C)]	170 to 389
Density (kg/m^3)	8960
Specific Heat [J/(kg °C)]	402 to 495
Latent Heat (J/kg)	2.05×10^5
Liquidus Temperature (°C)	1083
Solidus Temperature (°C)	1083

Table III. Physical Parameters of He and Ar

Parameter (Unit)	He	Ar
Thermal Conductivity [W/(m °C)]	0.16	0.02
Density (kg/m^3)	0.15	1.51
Viscosity (Pa s)	2.10×10^{-5}	2.42×10^{-5}
Specific Heat [J/(kg °C)]	5193.30	520

From Eq. [11], it can be observed that the temperature of cell $(i,\ j,\ k)$ at time $p + 1$ is influenced by the surrounding six cells and the temperature of the cell itself at time p. The sum of their coefficients is equal to 1, indicating that the temperature at time $p + 1$ in cell (i, j, k) can be considered as a weighted balance of these seven cells. To ensure that the computed results of the explicit difference scheme are physically meaningful, the coefficients of the seven cells' temperatures at time p should not be less than zero. Additionally, in order to guarantee the stability of the difference equation, the coefficient of $T^p_{i,j,k}$ should be greater or equal to zero, $i.e.$, the coefficient of $T^p_{i,j,k}$ in Eq. [11] should be ≥ 0. The stability condition for the difference equation in the three-dimensional spherical coordinate system can be expressed as follows:

$$\Delta\tau \leq \frac{1}{\alpha\left[\frac{2r^2_{i,j,k}+\frac{\Delta r^2}{2}}{\left(r_{i,j,k}\cdot\Delta r\right)^2}+\frac{\left(\sin\left(\theta_{i,j,k}+\Delta\theta/2\right)+\sin\left(\theta_{i,j,k}-\Delta\theta/2\right)\right)}{\sin\theta_{i,j,k}\left(r_{i,j,k}\Delta\theta\right)^2}+\frac{2}{\left(r_{i,j,k}\cdot\sin\theta_{i,j,k}\cdot\Delta\varphi\right)^2}\right]}. \quad [13]$$

Determine the space and time step based on the above conditions.

E. *Experimental Conditions and Physical Parameters*

The material prepared in this study is TU2 Oxygen-Free Copper, and the protective gas is helium or argon. The physical parameters are shown in Tables II and III, respectively. The experimental conditions and calculation parameters are shown in Table IV.

Table IV. Experimental Conditions and Computational Parameters

Parameter (Unit)	Value
Particle Diameter (μm)	150, 200, 300, 400
Gas Temperature (°C)	20
Wall Temperature (°C)	20
Initial Temperature (°C)	1103
Initial Velocity (m/s)	2, 3, 4

Considering computational accuracy and efficiency, the radial direction is divided into 20, 22, 24, and 26 grids depending on the particle diameter, with Δr approximately equal to 3.75, 4.55, 6.25, and 7.69 μm, respectively. In the zenith angle and azimuthal angle directions, five grids are used. The time step $\Delta\tau$ is set to 8.75×10^{-10} s, satisfying Eq. [13].

IV. RESULTS AND DISCUSSION

A. *Temperature Variation During Particle Cooling*

Without considering supercooling of the melt, the solidification of pure metal can be divided into three stages: (1) The first stage is the liquid superheating stage. Due to the temperature difference between the droplet and the cooling environment, heat exchange occurs between them, causing the temperature of the droplet to gradually decrease until it reaches the melting point. During this process, the droplet remains entirely in the liquid phase, atoms in the metal gather together through thermal vibrations, forming small solidification nuclei. (2) The second stage is the nucleation and latent heat release stage. Once solidification nuclei are formed, metal atoms align themselves in an ordered manner along the lattice structure of the nuclei and begin to grow. While the solidification nuclei grow, the metal droplet starts solidifying from the outer region towards the center, accompanied by the release of latent heat, resulting in a constant temperature. (3) The third stage is the solid cooling stage. After the complete release of latent heat, the temperature at the center of the particle decreases below the melting point. The cooling rate of the particle increases, gradually cooling down to the ambient temperature.

Figure 4 shows the temperature variation during the cooling process of copper particles with different diameters (initial temperature T_0) at a velocity of 2 m/s in an Ar environment at standard atmospheric pressure. The surface temperature and center temperature of particles with the same diameter exhibit similar trends. The time
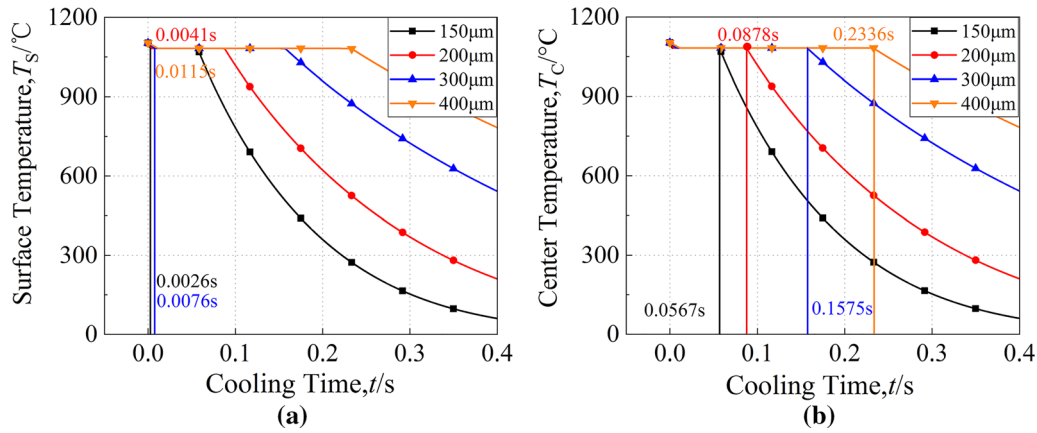
Fig. 4—Temperature variation of particles with different diameters with time: (*a*) Surface temperature; (*b*) Center temperature.
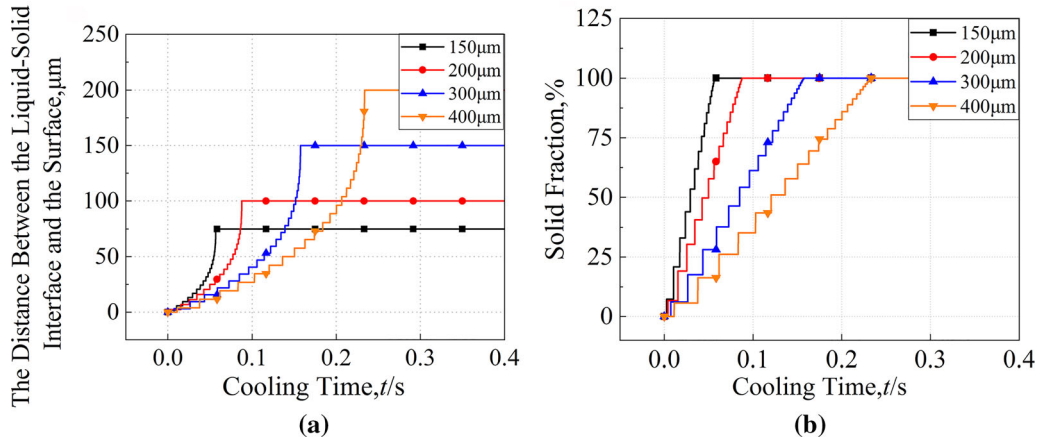

Fig. 5—Solidification characteristics of particles with different diameters: (*a*) Distance of the liquid–solid interface from the surface; (*b*) Solid fraction.

interval between the surface temperature decreasing to the melting point T_m (indicating the start of solidification) and the center temperature dropping below T_m (indicating the end of solidification) represents the solidification time of the particle. As shown in Figure 4(a), the initial moment of solidification is similar for particles with different diameters, however, the solidification time varies significantly with increasing diameter. Taking a 150 μm particle as an example, it begins solidifying at 0.0026 seconds and completes solidification at 0.0567 seconds, as seen in Figure 4(b), resulting in a solidification time of 0.0541 seconds. The solidification times for particles with diameters of 200, 300, and 400 μm are 0.0837, 0.1499, and 0.2221 seconds, respectively. Compared to the 150 μm particle, the solidification times increase by 54.7, 177.1, and 310.5 pct, respectively. Under the same cooling conditions, an increase in particle diameter leads to a slower temperature change at the surface and center, significantly reducing the cooling rate, thereby exerting a pronounced influence on the microstructure of the particles.

B. *Particle Solidification Process*

Figure 5 shows the solidification process of copper particles with different diameters during cooling in an Ar environment at a velocity of 2 m/s and standard atmospheric pressure. The solidification starts when the surface temperature of the droplet decreases to the melting point, and the liquid–solid interface progresses towards the center of the droplet. With increasing diameter, the volume of the phase-change region when the liquid–solid interface crosses the same distance becomes larger. This is reflected in Figure 5(a) as a longer time required for the liquid–solid interface to move the same displacement distance for larger diameters. The progression of the liquid–solid interface causes a change in the solid fraction of the particle, as shown in Figure 5(b). Smaller diameter particles solidify faster. The 150 μm particle completely solidifies at 0.0567 seconds, and based on Eq. [2], the particle only falls a distance of 0.1292 m.

During the rapid solidification process of micron-sized spherical particles, there exists a radial temperature difference between the surface and the center of the particles due to faster cooling at the surface and slower cooling in the interior. Figure 6(a) shows the
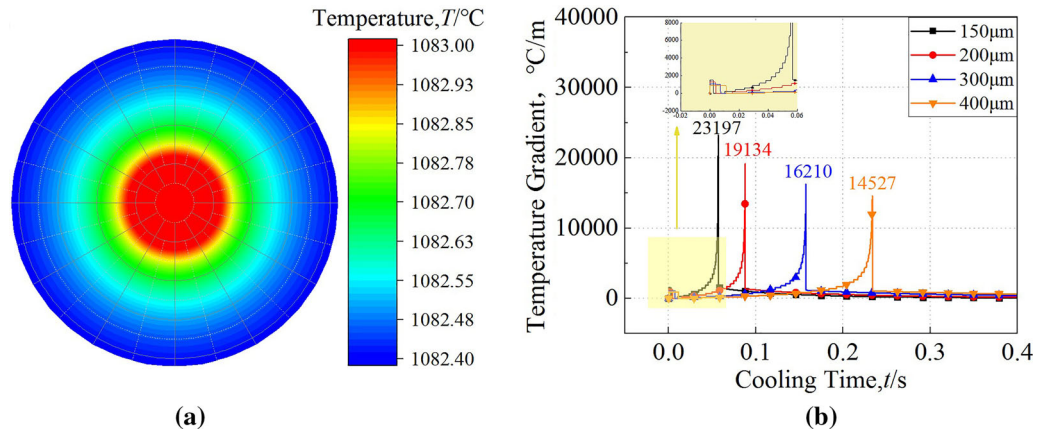
Fig. 6—Heat transfer process of particles with different diameters: (*a*) Temperature distribution at a characteristic moment (0.0850 s) during the solidification stage of a 200 *μ*m particle; (*b*) Temperature gradient.

cross-sectional temperature distribution of a 200 *μ*m particle at a characteristic moment (0.0850 seconds) during the solidification stage in an Ar environment at a velocity of 2 m/s and standard atmospheric pressure. The central region of the particle, under the influence of latent heat of crystallization, maintains a temperature near the melting point of the metal. The solidified shell on the surface rapidly decreases in temperature due to heat exchange with the environment, resulting in a three-stage temperature distribution pattern.

The radial temperature difference leads to temperature gradients, which in turn affect crystal nucleation and dendritic growth. Different growth directions and crystal structures of grains appear within the particle, and the size and distribution of these grains determine the particle's microstructure.

By expressing the ratio of the radial temperature difference to the particle radius, the variation of temperature gradient during the solidification process of particles with different diameters can be obtained, as shown in Figure 6(b). The droplet undergoes necking at the micro-orifice due to the combined effects of surface tension and vibration. The instantaneous temperature of entering the cooling chamber is uniformly distributed. Subsequently, heat exchange between the droplet surface and the environment begins, causing a decrease in surface temperature and a rapid increase in temperature gradient. Under the effect of thermal conduction within the droplet, the center temperature starts to decrease, leading to a reduction in the temperature gradient. When the surface temperature decreases to the melting point of the metal, surface solidification begins, accompanied by the release of latent heat of crystallization. The surface temperature no longer changes, while the center temperature gradually decreases to the melting point, resulting in a zero temperature gradient. After complete surface solidification, as no further latent heat is released, the temperature starts to decrease, and the liquid–solid interface begins to advance towards the center of the particle. The temperature in the central

Table V. Calculated Average Cooling Rates of Particles with Different Diameters

Particle Size (*μ*m)	Cooling Rate (°C/s)
150	7558.39
200	4749.39
300	2556.20
400	1678.08

region remains at the melting point, and the temperature gradient reappears, reaching its maximum at the instant when the particle is fully solidified at 0.0878 seconds. During the solid-phase cooling stage of the particle, the temperature gradient rapidly decreases due to heat exchange with the environment. The maximum temperature gradient for the 150 *μ*m particle can reach up to 23197 °C/m. With increasing diameter, the peak temperature gradients of different particles decrease, and the occurrence time of the peak is delayed.

C. *Particle Cooling Rate*

During the particle solidification process, the magnitude of the temperature gradient is mainly influenced by the thermal conductivity of the metal and the cooling rate. The thermal conductivity depends on the alloy type used, in order to obtain uniformly structured metal particles, we will focus on the particle cooling rate. Table V provides the calculated average cooling rates for metal particles with different diameters during cooling in an Ar environment at a velocity of 2 m/s and standard atmospheric pressure. Since the temperature remains constant during the solidification of pure metal, here we take the average cooling rate during the liquid droplet's superheating stage. By fitting the data in Table V, the relationship between the average cooling rate and the particle diameter can be obtained as shown in Figure 7 and Eq. [14].

$$\frac{\mathrm{d}T}{\mathrm{d}t} = 1.87 \times 10^7 (D)^{-1.56}. \quad [14]$$

In the experiment, TU2 oxygen-free copper was used to prepare metal particles, and the cooling gas was Ar gas. Figure 8(a) through (c) shows optical microscope images of the internal microstructures of Cu particles with different diameters obtained from the experiment. The particle diameters are 155.10, 247.60, and 355.40 μm, respectively. The average grain sizes (AGS) measured using the intercept method are 45.53, 61.67, and 67.98 μm, respectively. Under the same cooling environment, AGS increases with the increase in diameter. The specific measurement method can be described as follows: multiple straight lines were drawn on the particle cross section. The segments obtained by measuring the intersection points of these lines with grain boundaries represent individual grains. Finally, the average value of these line segments was taken as the average grain size, with at least 10 particles to ensure sufficient data.

Equation [15] relates the AGS observed to the diameter of the particles. By combining Eqs. [14] and [15], the relationship between AGS and cooling rate can be derived, as shown in Eq. [16]. This equation is highly consistent with the widely accepted relationship between secondary dendrite arm spacing and cooling rate (Eq. [17]). Since there is approximately an order of magnitude difference between the secondary dendrite arm spacing and AGS, the coefficient in Eq. [16] has a range of values that is roughly one order of magnitude larger than β.[18]
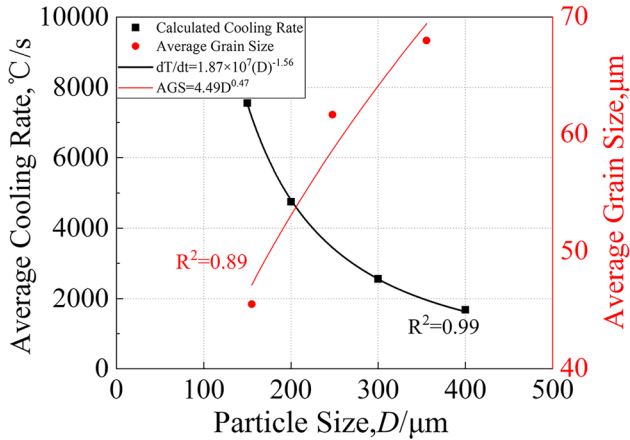

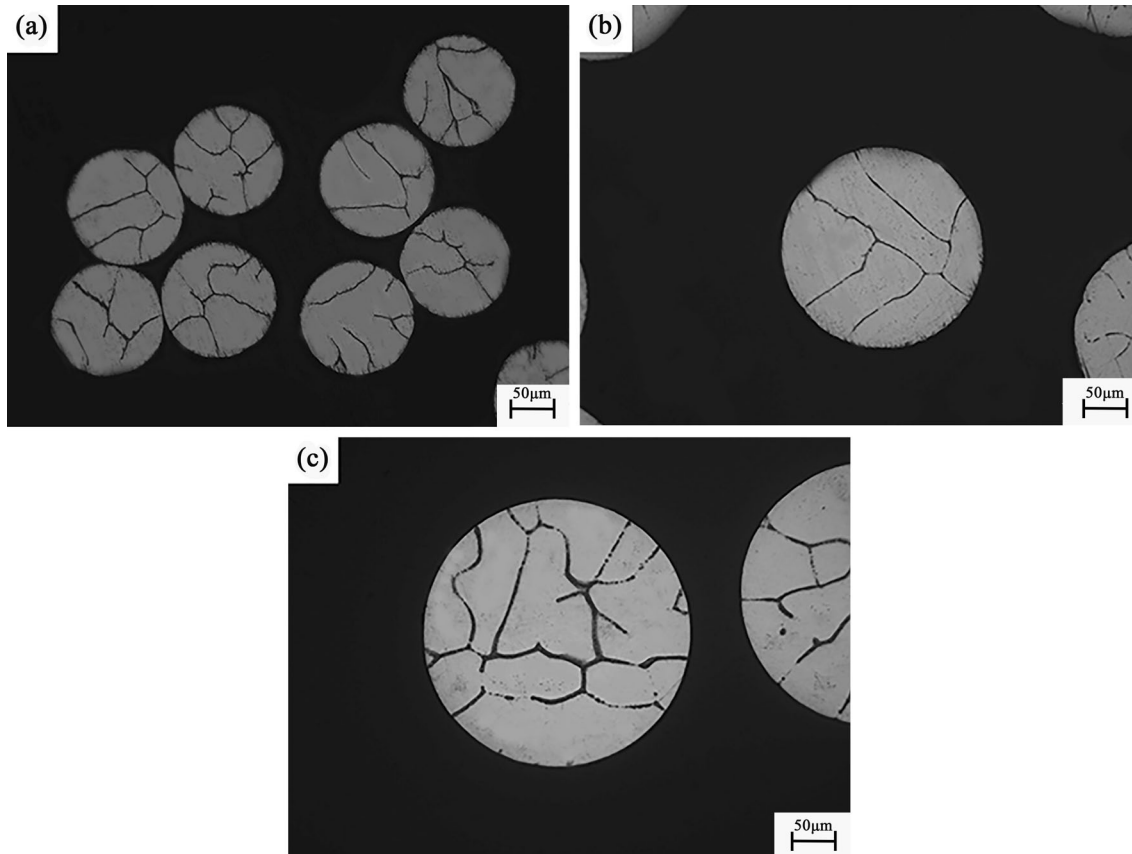Fig. 7—Variation of average cooling rate and average grain size of particles with particle size.

Fig. 8—OM photos of copper particles with different diameters in an Ar gas environment: (a) 115.1 μm; (b) 247.6 μm; (c) 355.4 μm.
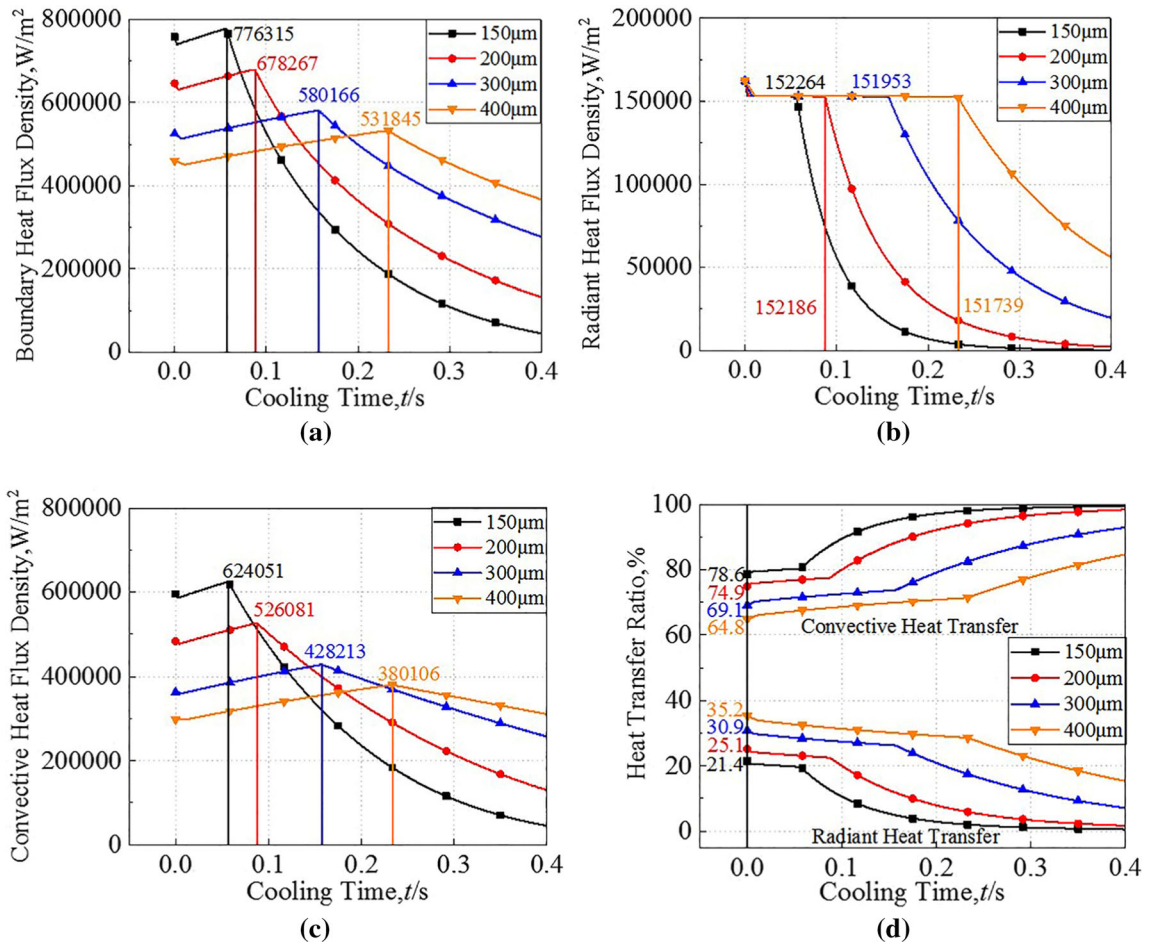
Fig. 9—The variation of surface heat flux density, radiative heat flux density, convective heat flux density, and the proportion of heat transfer over time for particles with different diameters: (*a*) Surface heat flux density; (*b*) Radiative heat flux density; (*c*) Convective heat flux density; (*d*) Heat transfer proportion.

$$AGS = 4.49D^{0.47} \qquad [15]$$

$$AGS = 694.63\left(\frac{\mathrm{d}T}{\mathrm{d}t}\right)^{-0.3} \qquad [16]$$

$$\lambda_2 = \beta\left(\frac{\mathrm{d}T}{\mathrm{d}t}\right)^{-1/3}. \qquad [17]$$

D. *Particle Convection Heat Transfer and Radiative Heat Transfer*

From Eq. [16], it can be inferred that achieving a sufficiently high cooling rate is crucial for producing particles with small average grain size or even amorphous structure. During particle cooling, heat is transferred to the environment through both convection and radiation mechanisms. Figure 9 presents the variation of surface heat flux density, radiant heat flux density, convective heat flux density, and the proportion of each

heat transfer mechanism to the total heat flux over time for particles with different diameters in an Ar gas environment with an initial velocity of 2 m/s and at a standard atmospheric pressure.

Based on Eqs. [6] through [10], it can be observed that the convection heat flux density depends not only on the temperature difference between the surface and the environment but also on the convective heat transfer coefficient. Increasing the diameter leads to a decrease in the convection heat flux density. On the other hand, the radiative heat flux density is only influenced by the fourth power difference between the surface temperature and the environment temperature. Under the combined effects of convection and radiation heat transfer mechanisms, the surface heat flux density exhibits a general trend of decrease-rise-decrease, as shown in Figure 9(c). Specifically, during the liquid overheating stage, as the temperature difference between the surface and the environment gradually decreases, the surface heat flux density decreases. Once nucleation and latent heat release occur, the surface temperature of the liquid droplet remains constant, resulting in a constant radiative heat flux density, as illustrated in Figure 9(b). The increase in particle velocity increases the convective heat

transfer coefficient, which is shown in Figure 9(a) as an increase in convective heat flux density and, consequently, an increase in the surface heat flux density. After the particle fully solidifies and enters the solid-phase cooling stage, the temperature difference between the particle and the environment rapidly decreases, causing a sharp decline in the surface heat flux density.

As the diameter increases, the peak value of the surface heat flux density gradually decreases, and the proportion of convection heat flux density to the total heat flux density at the initial moment decreases. The surface heat flux densities at the complete solidification moments for particles with diameters of 150, 200, 300, and 400 μm are 776,315, 678,267, 580,166, and 531,845 W/m^2, respectively. At the initial moment, the proportion of the convective heat flux of 400 μm particles to the total heat flux decreased from 78.6 pct of that of 150 μm particles to 64.8 pct as can be seen from Figure 9(d). Smaller particles have a larger surface area compared to their volume. Since heat transfer mainly occurs at the surface of particles, smaller particles have more surface area for heat exchange. Especially, based on Eqs. [8] through [10], the convective heat transfer coefficient significantly increases with the decrease of particle size. This means that, under the same temperature difference, smaller particles have a greater heat transfer effect and intensity, resulting in a higher proportion of convective heat flux density to the total heat flux. Because the temperature difference has a more significant impact on radiative heat transfer, it leads to a continuous decrease in the proportion of radiative heat transfer during the cooling process. Consequently, convection heat transfer becomes the dominant heat transfer mechanism during particle cooling. Increasing the convection heat flux density during the particle cooling process is beneficial for enhancing the cooling rate.

V. CONCLUSIONS

In this study, the cooling heat transfer and solidification characteristics of micrometer-sized spherical metal particles in the process of POEM were investigated. A numerical model and computational program were developed based on the finite difference method and a three-dimensional spherical coordinate system to describe the heat transfer and solidification processes of micrometer-sized spherical pure metal particles. The relationship between particle heat transfer behavior and the microstructure during solidification was analyzed by simulating temperature distribution and solidification progress. The following conclusions were drawn:

(1) The solidification process of pure metal particles consists of three stages: liquid superheating stage, nucleation and solidification with latent heat release stage, and solid cooling stage. The numerical values and trends of surface temperature and center temperature of the particles are similar. When the metal particles are cooled in an Ar gas environment at an initial velocity of 2 m/s and a standard atmospheric pressure, the solidification time increases with the diameter. A 400 μm particle takes 0.2221 seconds to solidify, which is more than three times longer than the solidification time of a 150 μm particle. The maximum cooling rate of the 150 μm particle is 7720 °C/s and decreases significantly with increasing diameter.

(2) At specific moments during the solidification process, the cross-sectional temperature of the particles exhibits a three-segment variation and significant radial temperature differences, resulting in large temperature gradients. The temperature gradient of a 150 μm particle can reach 23197 °C/m at a falling distance of 0.1292 m. The peak temperature gradient is negatively correlated with the diameter, with the peak temperature gradient of a 400 μm particle being only 14527 °C/m. The temperature gradient determines the microstructure of the particles, and understanding and controlling the temperature gradient are of great significance for the study and application of particle microstructures.

(3) The magnitude of the temperature gradient is controlled by both the cooling rate and the metal thermal conductivity. By relating the actual grain size to the calculated average cooling rate based on particle diameter, a relationship between grain size and cooling rate is obtained, which is consistent with the relationship between secondary dendrite arm spacing and cooling rate. The average cooling rate of a 150 μm particle is 7558.39 °C/s, and the grain size is approximately 44.64 μm.

(4) During different stages of particle cooling, the proportions of convective and radiative heat flux density to the total heat flux density vary. As the diameter increases, the proportion of convective heat flux density decreases at the initial stage. The proportion of convective heat flux density to total heat flux density for 150 to 400 μm particles ranges from 64.8 to 78.6 pct at the initial stage. As the cooling process progresses, the proportion of convective heat transfer increases, indicating that convective heat transfer is the dominant heat transfer mechanism in particle cooling.

CONFLICT OF INTEREST

On behalf of all authors, the corresponding author states that there is no conflict of interest.

REFERENCES

1. B. Blakey-Milner, P. Gradl, G. Snedden, M. Brooks, J. Pitot, E. Lopez, M. Leary, F. Berto, and A. du Plessis: *Mater. Des.*, 2021, vol. 209, p. 110008.
2. W.E. Frazier: *J. Mater. Eng. Perform.*, 2014, vol. 23, pp. 1917–28.
3. H. Jeong, K.D. Min, C.-J. Lee, J.-H. Kim, and S.-B. Jung: *Microelectron. Reliab.*, 2020, vol. 112, p. 113918.
4. A. Szcześ, L. Hołysz, and E. Chibowski: *Adv. Colloid Interface Sci.*, 2017, vol. 249, pp. 321–30.
5. K.M. Em Akra, M. Akkaş, M. Boz, and E. Seabra: *Russ. J. Non-Ferrous Met.*, 2020, vol. 61, pp. 332–45.
6. M. Zhang and Z. Zhang: *Mater. Today Commun.*, 2020, vol. 25, p. 101423.
7. K. Kassym and A. Perveen: *Mater. Today: Proc.*, 2020, vol. 26, pp. 1727–33.
8. L. Ning, S. Luo, Z. Li, L. He, and H. Li: *Heat Mass Transf.*, 2022, vol. 58, pp. 1247–62.
9. S. Hoeges, A. Zwiren, and C. Schade: *Met. Powder Rep.*, 2017, vol. 72, pp. 111–17.
10. L.C. Zhang, D. Klemm, J. Eckert, Y.L. Hao, and T.B. Sercombe: *Scripta Mater.*, 2011, vol. 65, pp. 21–24.
11. B. Li, W. Zhou, and L. Liu: *Rare Met. Mater. Eng.*, 2011, vol. 40, pp. 257–60.
12. Y. Yingxue, G. Shengdong, and C. Chengsong: *J. Mater. Process. Technol.*, 2004, vol. 146, pp. 389–95.
13. S.K. Pillai and T. Ando: *Int. J. Therm. Sci.*, 2009, vol. 48, pp. 1494–500.
14. K. Takagi, S. Masuda, H. Suzuki, and A. Kawasaki: *Mater. Trans.*, 2006, vol. 47, pp. 1380–85.
15. Y. Guo, C. Li, N. Deng, H. Sun, S. Feng, Y. Zhang, X. Li, E. Ci, and J. Li: *Mater. Today Commun.*, 2022, vol. 30, p. 103110.
16. W. Dong, S. Masuda, K. Takagi, and A. Kawasaki: *Mater. Sci. Forum*, 2007, vol. 534–536, pp. 149–52.
17. B. Zhao, W. Dong, H. Ji, Q. Zhang, L. Zhang, M. Wu, Q. Zhai, and Y. Gao: *MRS Commun.*, 2017, vol. 7, pp. 709–14.
18. K.-F. Li, Y.-H. Zhang, C.-J. Song, and Q.-J. Zhai: *Adv. Manuf.*, 2016, vol. 4, pp. 150–56.
19. N. Yodoshi, R. Yamada, A. Kawasaki, and A. Makino: *J. Alloys Compd.*, 2015, vol. 643, pp. S2–S7.
20. D. Gianoglio, N. Ciftci, S. Armstrong, V. Uhlenwinkel, and L. Battezzati: *Metall. Mater. Trans. A*, 2021, vol. 52A, pp. 3750–58.
21. M. Li, H. Wang, N. Yan, and B. Wei: *Sci. China: Technol. Sci.*, 2018, vol. 61, pp. 1021–30.
22. K.-C. Chang and C.-M. Chen: *Int. J. Heat Mass Transf.*, 2001, vol. 44, pp. 1573–83.
23. Z.-Q. Pi, X. Lu, Y. Wu, L.-N. Wang, C.-C. Jia, X.-H. Qu, W. Zheng, L.-Z. Wu, and Q.-L. Shao: *Int. J. Miner. Metall. Mater.*, 2017, vol. 24, pp. 657–69.
24. N. Madhavan, G.A. Brooks, M.A. Rhamdhani, B.K. Rout, A. Overbosch, K. Gu, A. Kadrolkar, and N. Dogan: *Metall. Mater. Trans. B*, 2021, vol. 52B, pp. 4141–56.
25. S.M. Mirabedin and F. Farhadi: *Int. J. Refrig.*, 2017, vol. 73, pp. 219–25.